nature communications

Article

https://doi.org/10.1038/s41467-025-60573-z

Boosting responsivity and speed in 2D material based vertical p-i-n photodiodes with excellent self-powered ability

Received: 14 July 2024

Accepted: 28 May 2025

Published online: 01 July 2025

Check for updates

Maoxin Tian[1], Yufan Wang[2], Tianjiao Zhang[1], Cheng Zhang[1], Jialei Miao[1], Zheng Bian[1], Xiangwei Su[1], Zongwen Li[1], Jian Chai[1], Anran Wang[3], Fengqiu Wang[4], Bin Yu[1], Yang Xu[1], Yang Chai[5], Xiao Wang[2] & Yuda Zhao[1]

Vertical p-i-n junctions are key components for optoelectronics to achieve fast response speed. However, a critical bottleneck lies in the complex fabrication techniques and the performance tradeoff between high responsivity and fast speed, especially under self-powered mode. Here, we illustrate the superiority of 2D materials-based vertical p-i-n photodiodes with maximized optical absorption in intrinsic layer (high responsivity), the efficient photocarrier separation (self-power ability), and the high-field drift velocity (fast speed). By optimizing the photocarrier generation/transfer dynamics via doping and thickness engineering, our device with zero voltage bias achieves high built-in electric field, leading to a high responsivity of 0.388 A W^{-1} and an *EQE* of 90.5% at 532 nm, a short intrinsic response time of sub-10 ps, a fast switching response time of 23 ns, and a high power conversion efficiency of 6.5%. Our work lays the foundation to resolve the responsivity-speed dilemma without the constraint of lattice mismatch.

Serving as functional components for the conversion of optical signals into electrical signals, photovoltaic devices have received extensive attention in modern optoelectronic technology[1–6]. Si photovoltaic devices, e.g., photodetectors and solar cells, widely employ a vertical p-type/intrinsic/n-type (p-i-n) junction, where an intrinsic layer is sandwiched between the n-type and p-type regions of a p-n junction, to achieve saturated light absorption and a fast response speed. Due to the relatively low optical absorption coefficient of silicon (e.g., $8 \times 10^3 cm^{-1}$ at 532 nm)[7], the intrinsic region of a silicon p-i-n photodiode needs to be quite thick to fully absorb the incident light, ranging from several micrometers to a few hundred micrometers. However, the large thickness results in the reduced built-in electric field and the long drift/diffusion length, limiting the speed. This is the long-standing responsivity-speed dilemma (Fig. 1a). Furthermore, Si-based p-i-n photodiodes usually require a large bias voltage, which greatly increases power consumption. The ultimate target is the simultaneous boosting of responsivity and speed in self-powered p-i-n photodiodes.

Two-dimensional (2D) materials with the strong light-matter interaction[8–10], are currently the subject of intense investigation as the optoelectronic responsive layer prompted by the need for superior-performance photodiodes in terms of sensitivity, detection speed, as well as flexibility and self-powered ability. Owing to the high optical absorption coefficient (e.g., $3.38 \times 10^5 cm^{-1}$ at 532 nm for WSe_2, 40 times higher than Si)[11], 2D materials allow for significantly reduced thickness of intrinsic layer, which can greatly decrease the drift/diffusion length and amplify the built-in electric field. Until now, the design

[1]College of Integrated Circuits, ZJU-Hangzhou Global Scientific and Technological Innovation Centre, Zhejiang University, Hangzhou, China. [2]Key Laboratory for Micro-Nano Physics and Technology of Hunan Province, College of Materials Science and Engineering, School of Physics and Electronics, Hunan University, Changsha, China. [3]School of Science, Nanjing University of Posts and Telecommunications, Nanjing, China. [4]School of Electronic Science and Engineering, Nanjing University, Nanjing, China. [5]Department of Applied Physics, The Hong Kong Polytechnic University, Hong Kong, China.
e-mail: yudazhao@zju.edu.cn

https://doi.org/10.1038/s41467-025-60573-z

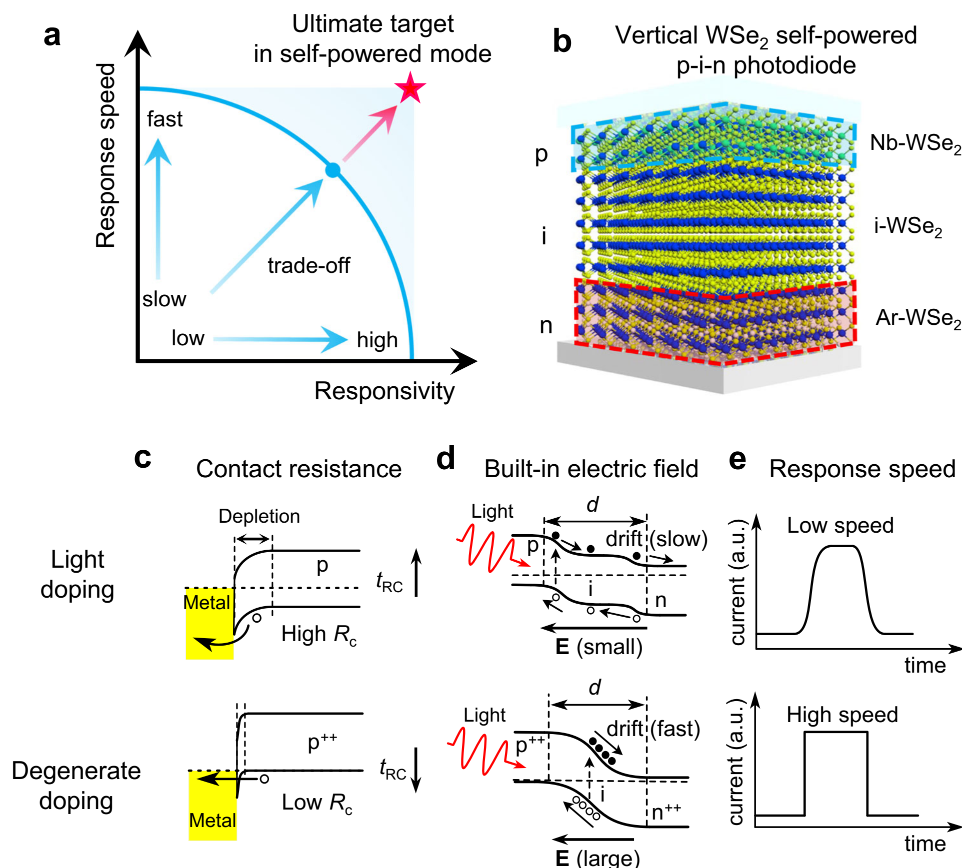

Fig. 1 | Concept of the high-speed vertical WSe_2 p-i-n photodiode. **a** Development target for self-powered photodetectors. Existing photodetectors are invariably constrained by a speed-responsivity trade-off (blue solid line), manifesting as either rapid response with limited responsivity, high responsivity with sluggish response, or intermediate performance in both metrics. The ultimate target (red five-pointed star) of self-powered photodetector is the concurrent realization of enhanced responsivity and accelerated response speed. **b** Schematic diagram of the vertical WSe_2 p-i-n photodiode. Niobium (Nb) doped WSe_2 (Nb-WSe_2, blue dash line region), pristine WSe_2 (i-WSe_2) and Argon (Ar) plasma treated WSe_2 (Ar-WSe_2, red dash line region) are used as p type/intrinsic/n type layer, respectively. P-type doping is achieved through niobium substitutional doping, while n-type doping is realized by generating selenium vacancies via Ar plasma bombardment of the WSe_2 surface. **c** Band diagrams of metal contact with lightly p-doped (upper) and degenerately p-doped (bottom) semiconductor, respectively. Light doping creates a wide and high potential barrier, resulting in large contact resistance and consequently increased RC time (t_{RC}). In contrast, degenerate doping produces a narrow barrier and direct tunneling transport of carriers, yielding lower contact resistance and reduced RC time. **d** Band diagrams of the p-i-n photodiode with lightly doped (upper) and degenerately doped (bottom) p-type layer under light illumination, respectively. Light doping creates a narrow depletion region in the intrinsic layer with relatively weak electric field, resulting in low drift velocity of photo-generated carriers under illumination. In contrast, degenerate doping enables complete depletion of the intrinsic layer, where the strong electric field facilitates high-speed carrier drift. **e** Schematic diagram of the photodiode response time with lightly doped (upper) and degenerately doped (bottom) p-type layer, respectively. Light doping results in a high RC time and slow carrier drift, leading to a sluggish detector response speed, as evidenced by the gradual transition in the current-time (*I-t*) curve. In contrast, degenerate doping reduces the RC time and accelerates carrier drift, enabling fast detector response with sharp transitions in the *I-t* curve.

of 2D materials-based self-powered photodiodes has largely relied on a lateral metal–2D materials–metal phototransistor or a lateral p-n junction[12–14]. However, the long transport length leads to the small built-in electric field, the low carrier drift speed, and the long diffusion length, resulting in a slow response speed in self-powered mode, which is not ideal for efficient photon harvesting and photon-current conversion. In contrast, the vertical structure with a short transport length greatly enhances the built-in electric field and reaches the saturation drift velocity, achieving high-speed carrier drift and the fast response speed. Therefore, it is essential to fabricate 2D materials based vertical p-i-n photodiodes, exploring the photocarrier generation/transfer dynamics to solve responsivity-speed dilemma. The major challenges include the achievement of high-quality contact (degenerate doping) and the optimization of p-type/intrinsic/n-type layer thickness, leading to the maximized optical absorption in intrinsic layer (high responsivity), the efficient photocarrier separation (high built-in electric field and self-powered ability), and the saturation drift velocity (fast speed).

In this work, we utilize WSe_2 thin layers to construct high-performance vertical p-i-n photodiode by optimizing the photocarrier generation and transfer dynamics. The Nb-doped WSe_2 with high hole concentration of $2.65 \times 10^{21}\,cm^{-3}$ as the degenerate p-doped layer effectively reduces the contact resistance and boosts the built-in electric field, leading to the efficient photocarrier separation/collection, the high-field drift velocity, and short intrinsic response time. The ultimate thickness downscaling of the 2D Nb-doped WSe_2 p-type layer results in the maximized photocarrier generation in the intrinsic WSe_2 layer, contributing to high responsivity and the nearly ideal external quantum efficiency (*EQE*). The fabricated vertical WSe_2 p-i-n photodiode exhibits a current rectification ratio of 6×10^6. Under self-powered condition (zero voltage bias), the device displays a high responsivity of $0.388\,A\,W^{-1}$ (corresponding to *EQE* of 90.5%), a high specific detectivity of 1×10^{12} Jones, a short intrinsic response time down to sub-10 picoseconds, and a fast switching response time of 23 ns. Furthermore, the photodiode achieves a high fill factor of 0.629

and a power conversion efficiency of 6.5%. Our strategy resolves the dilemma between high responsivity and fast speed via the construction of van der Waals vertical p-i-n photodiodes.

Results

Degenerate doping to speed up the vertical WSe_2 p-i-n photodiodes

Figure 1b illustrates the schematic structure of vertical WSe_2 p-i-n photodiode, where an intrinsic WSe_2 layer is sandwiched between the p-doped and the n-doped layers. The intrinsic layer is responsible for the optical absorption and the doping layers act as the charge transport layer. To achieve the fast response speed, we need to optimize the limiting factors of the response time (t_r) in the photodiode, including time constant (t_{RC}), drift time (t_{Drift}), and diffusion time ($t_{Diffusion}$), which can be expressed as follows[15–17]:

$$t_r = \sqrt{t_{RC}^2 + t_{Drift}^2 + t_{Diffusion}^2} \quad (1)$$

The t_{RC} represents the RC time delay of the external wires/circuits, which can be reduced by forming degenerate doping to decrease the contact resistance R_c (Fig. 1c). The t_{Drift} is the time it takes for photogenerated carriers within the depletion region to reach the electrode driven by an electric field. Assuming that photocarriers generated in the middle of the channel, the drift time can be calculated by the equation of $t_{Drift} = d/v = d/\mu\mathbf{E}$, where v is the drift velocity, d is the width of the depletion region, μ is the carrier mobility, and $\mathbf{E}$ is the electric field strength. A large electric field ($\mathbf{E}$) and a small depletion width d are preferred to achieve fast photocarrier separation (Fig. 1d), which require a high degenerate doping level with low contact resistance in doped regions and a relatively thin thickness of the intrinsic layer. Finally, the $t_{Diffusion}$ refers to the time it takes for photogenerated carriers in the neutral region to diffuse into the depletion region. In a fully depleted vertical photodiode, where the depletion region extends across the entire device, the diffusion time can be ignored. Therefore, the increase of the doping concentration in the p- and n-type layers is essential to achieve a high electric field across the depletion region and a low contact resistance, leading to the ultrafast separation of photogenerated carriers and the short interfacial transfer time, which can significantly increase the response speed (Fig. 1e).

In our work, the pristine WSe_2 serves as the intrinsic layer (i-WSe_2), which is lightly n doping. The electron concentration of $6.56 \times 10^{14}\,cm^{-3}$ is obtained by the four-probe testing method (Supplementary Fig. 1 and Methods section). The low carrier concentration of i-WSe_2, combined with the Fermi level pinning effect, makes it challenging to form Ohmic contacts. As shown in Supplementary Fig. 2, the output curves of the pristine WSe_2 field-effect transistor (FET) exhibit significant nonlinearity, indicating the presence of a noticeable Schottky barrier between i-WSe_2 and the metal electrodes.

To fabricate p-i-n photodiode, it requires the feasible doping strategies. Here, argon (Ar) plasma etching has been employed to introduce n-type doping on i-WSe_2. The doping mechanism is that Ar plasma bombardment creates numerous Se vacancies and a sub-stoichiometric WSe_2 ($WSe_{2\text{-}y}$) is formed. Abundant Se vacancies endow the interfacial $WSe_{2\text{-}y}$ layer with excellent electron donor capacity, thereby enabling electron doping of WSe_2, which is similar to surface-charge-transfer p doping of WSe_2 via WO_3 coating[18–20]. As shown in Supplementary Fig. 2, the output curve of the pristine WSe_2 FET after Ar plasma treatment is noticeably linear, indicating that the Ar plasma can realize electron doping and improve the contact quality. The power and the time of Ar plasma process has been optimized, which is 100 W and 90 s (Supplementary Fig. 3). To assess the depth of $WSe_{2\text{-}y}$ doping, we tested threshold voltage variation ΔV_{th} of WSe_2 FET with varying thicknesses after Ar plasma treatment (Supplementary Fig. 4). We found that as the thickness increased, the estimated carrier concentration decayed exponentially (Supplementary Fig. 5). The thickness at which the concentration decays to 1/e is considered the thickness of the n-region. From the fitting curve, the thickness of n-doped layer is about 12 nm, where the electron concentration is about $2.5 \times 10^{18}\,cm^{-3}$. For ease of description, we refer to $WSe_{2\text{-}y}$ and its doped WSe_2 as Ar-WSe_2. As shown in Fig. 2a, the FET with Ar plasma treatment in the contact area exhibits a high current on-off ratio (I_{on}/I_{off}) exceeding 10^6. The maximum drain current (I_{ds}) is 1.63 μA·μm^{-1} at drain voltage $V_{ds} = 1\,V$ and back gate voltage $V_{bg} = 60\,V$. Additionally, the output curves exhibit a high linearity, indicating the formation of high-quality contact between Ar-WSe_2 and metal electrode.

Nb doped WSe_2 (Nb-WSe_2) works as the degenerate p-type doping layer, where the atomic ratio of Nb is 5%. Hall effect measurements using van der Pauw sample configuration demonstrate that the carrier concentration of Nb-WSe_2 is $2.65 \times 10^{21}\,cm^{-3}$ (Supplementary Figs. 6 and 7). This high hole concentration can contribute to the low contact resistance and the high built-in electric field in WSe_2 p-i-n photodiode. We further fabricated a WSe_2 FET with Nb-WSe_2 as contact electrodes (optical image in Supplementary Fig. 8). The transfer and output curves in Fig. 2b demonstrate a significant hole transport behavior over a wide range of back gate voltage (V_{bg}). The FET exhibits an extremely high I_{on}/I_{off} exceeding 10^8. The maximum I_{ds} is 4.17 μA·μm^{-1} at drain voltage $V_{ds} = 1\,V$ and $V_{bg} = -60\,V$. Moreover, I_{ds} shows a linear relationship with V_{ds}, indicating that p-type Ohmic contact is achieved. Improved ohmic contact between the electrode and the doped layer indicates that doping can indeed enhance contact quality, and this effect is also effective in vertical structures.

The vertical Nb-WSe_2/WSe_2/Ar-WSe_2 p-i-n photodiode has been fabricated via dry transfer technique and the detailed fabrication process has been described in Methods section and Supplementary Fig. 9. We used transmission electron microscopy (TEM) to characterize the interface quality of the p-i-n diode. The cross-sectional TEM image (Fig. 2c) shows a distinct layered structure and high-quality van der Waals interfaces, with the thickness of monolayer i-WSe_2 and Nb-WSe_2 being approximately 0.7 nm. The region treated with Ar plasma exhibits a clear amorphous structure ($WSe_{2\text{-}y}$), which is non-conductive (Supplementary Fig. 10), and the thickness is about 4 nm. Under dark, the diode displays a unidirectional conductivity with a low reverse saturation current density of $1.29 \times 10^{-3}\,mA\,cm^{-2}$ and a high rectification ratio of 5.9×10^6 ($V_{ds} = \pm 2\,V$), as shown in Fig. 2d. The photoresponse characteristics of the vertical WSe_2 p-i-n photodiode have been tested under 532 nm laser with different power density (P_{in}). When the optical power density is over 29730 mW·cm^{-2}, the maximum open-circuit voltage (V_{oc}) of 0.7 V is achieved. The current-power relationship of the photodiode can be described as power-law: $I \propto P^{\alpha}$. Within the range of P_{in} from 0.0016 to 29730 mW cm^{-2}, the short-circuit current density (J_{sc}) exhibits excellent linear correlation with P_{in}, with exponent α close to 1 (α = 0.98), indicating that the photovoltaic effect is dominant (Fig. 2e). The contact resistance (series resistance) in the vertical Nb-WSe_2/WSe_2/Ar-WSe_2 p-i-n photodiode, estimated from the dark *I-V* curve, is 9 kΩ, and can even reach as low as 1 kΩ (Supplementary Note 1 and Supplementary Fig. 11). Therefore, we ascribe this excellent V_{oc} to the large Fermi energy gradient across p-i-n junction and the low voltage drop at the contact regions, which stem from the high concentration in Nb-WSe_2 and Ar-WSe_2, minimizing contact resistance. Supplementary Fig. 12 illustrates the band alignment diagram of the vertical p-i-n photodiode. Due to the high carrier concentration in Nb-WSe_2 (three orders of magnitude higher than that in Ar-WSe_2), the depletion region is entirely concentrated in i-WSe_2 and Ar-WSe_2. When the device is forward biased, the depletion region narrows, the potential barrier for carriers decreases, and the current starts to increase. Conversely, when the device is reverse biased, the depletion region begins to extend into Ar-WSe_2. When the reverse bias is much greater than 0 V, Ar-WSe_2 becomes fully depleted, significantly increasing the reverse tunneling current. When the device is under light and no bias, the depleted i-WSe_2 fully absorbs photons and

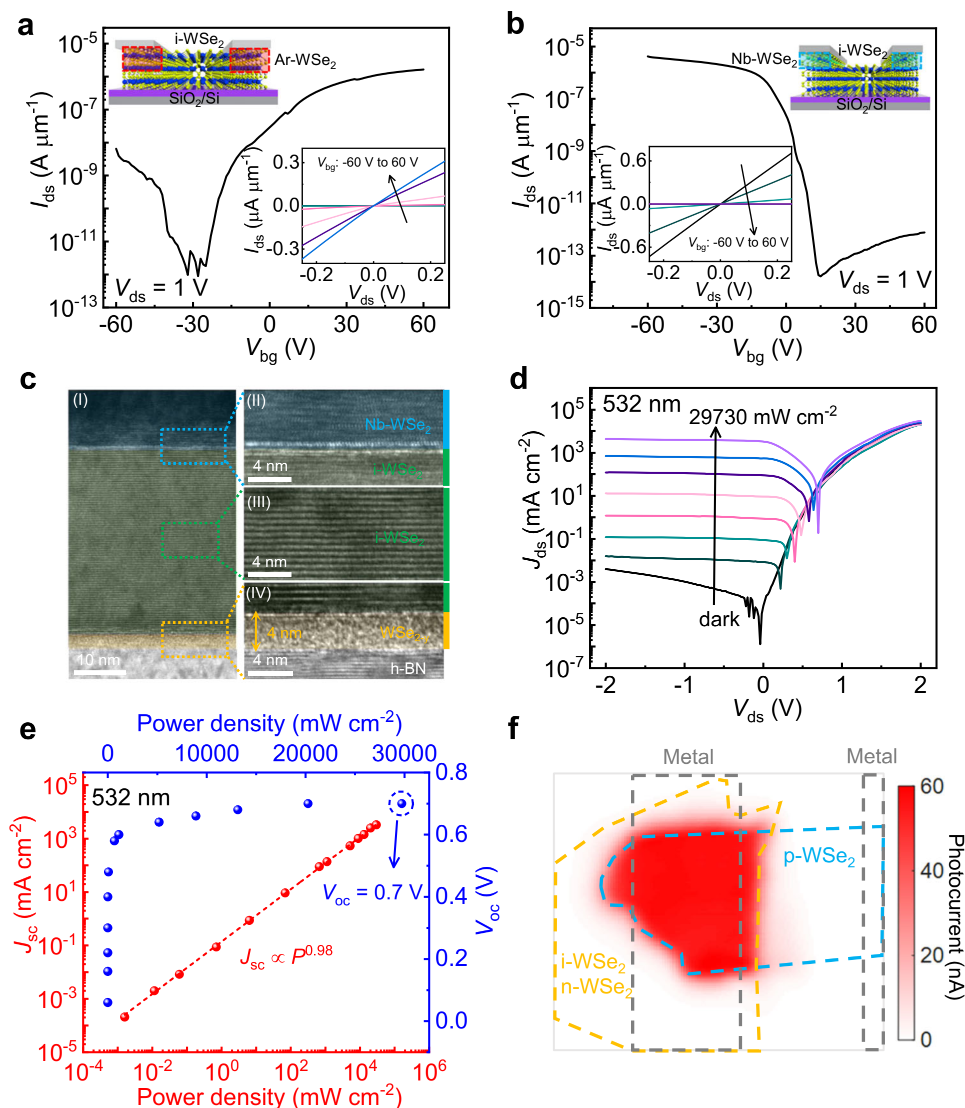

Fig. 2 | Optoelectronic characteristics of the p-i-n photodiode with degenerated doping layer. a Transfer curve, output curve and structure schematic of WSe_2 FET with Ar-WSe_2 (red dash line region) contact. **b** Transfer curve, output curve and structure schematic of WSe_2 FET with Nb-WSe_2 (blue dash line region) contact. **c** Transmission electron microscope (TEM) image of vertical WSe_2 p-i-n junction. Pristine WSe_2 exhibits a distinct layered crystalline structure, while Ar plasma-treated WSe_2 demonstrates a clearly amorphous phase (denoted as WSe_{2-y}) with a thickness of 4 nm. **d** Current density (J_{ds}) – V_{ds} curves of WSe_2 p-i-n photodiode under 532 nm laser illumination with different power density (P_{in}). **e** Power dependent open-circuit voltage (V_{oc}) and short-circuit current density (J_{sc}). The maximum V_{oc} is 0.7 V, and J_{sc} exhibits linear correlation with P_{in} (J_{sc} $P^{0.98}$). **f** Short-circuit SPCM image of the p-i-n photodiode using a 488 nm focused laser with power of 1.73 μW. The photocurrent originates from the overlapping area of Ar-WSe_2 (orange dash line), i-WSe_2 (orange dash line) and Nb-WSe_2 (blue dash line). The gray dash lines are Ag metal electrodes.

converts them into photogenerated electron-hole pairs, which are quickly separated under the large built-in electric field. Since the thickness of WSe_{2-y} is relatively thin (~4 nm), the carriers can easily tunnel through the WSe_{2-y} layer and reach the electrode to generate photocurrent. To further verify the mechanism of our device, scanning photocurrent mapping (SPCM) is used to obtain the photocurrent distribution in Fig. 2f. Under zero bias condition, the photosensitive region corresponds to the overlapping area of Ar-WSe_2, i-WSe_2 and Nb-WSe_2. It confirms that the photocurrent originates from the generation of photoexcited charge carriers in the i-WSe_2 layer, followed by the transfer of these charges to the Ar-WSe_2 and Nb-WSe_2, rather than the contact region around the electrode/WSe_2 interface in lateral photovoltaic devices. Furthermore, Fig. 2f shows negligible response at the Ar-WSe_2 and i-WSe_2 interface, indicating that the depletion region is contributed by the junction between Nb-WSe_2 and i-WSe_2. The primary function of Ar-WSe_2 is to improve contact and enhance carrier collection efficiency. Therefore, the thickness of Ar-WSe_2 does not affect the response speed and responsivity of the p-i-n device.

To obtain the intrinsic response time of the vertical WSe_2 p-i-n photodiode and exclude the impact of RC delay time, we performed the time-resolved photocurrent (TRPC) measurement by exciting the device with a pair of ultrashort optical pulses (80 fs, 780 nm) separated by a variable time delay (Fig. 3a). TRPC technique exploits the photocurrent dynamics of the vertical WSe_2 p-i-n photodiode under the nonlinear power dependence of the photocurrent. Figure 3b shows that when average laser pulse intensities exceed 882 W cm^{-2}, our device exhibits the significant nonlinear power dependence ($J_{sc} \propto P^{0.68}$). The observed sub-linearity probably originates from saturable absorption. With the presence of the pump beam, the photocurrent has been suppressed at zero delay time, further indicating the saturation of the photocurrent. We plotted the normalized photocurrent as a function of the delay time with different WSe_2 thickness (L)

 https://doi.org/10.1038/s41467-025-60573-z

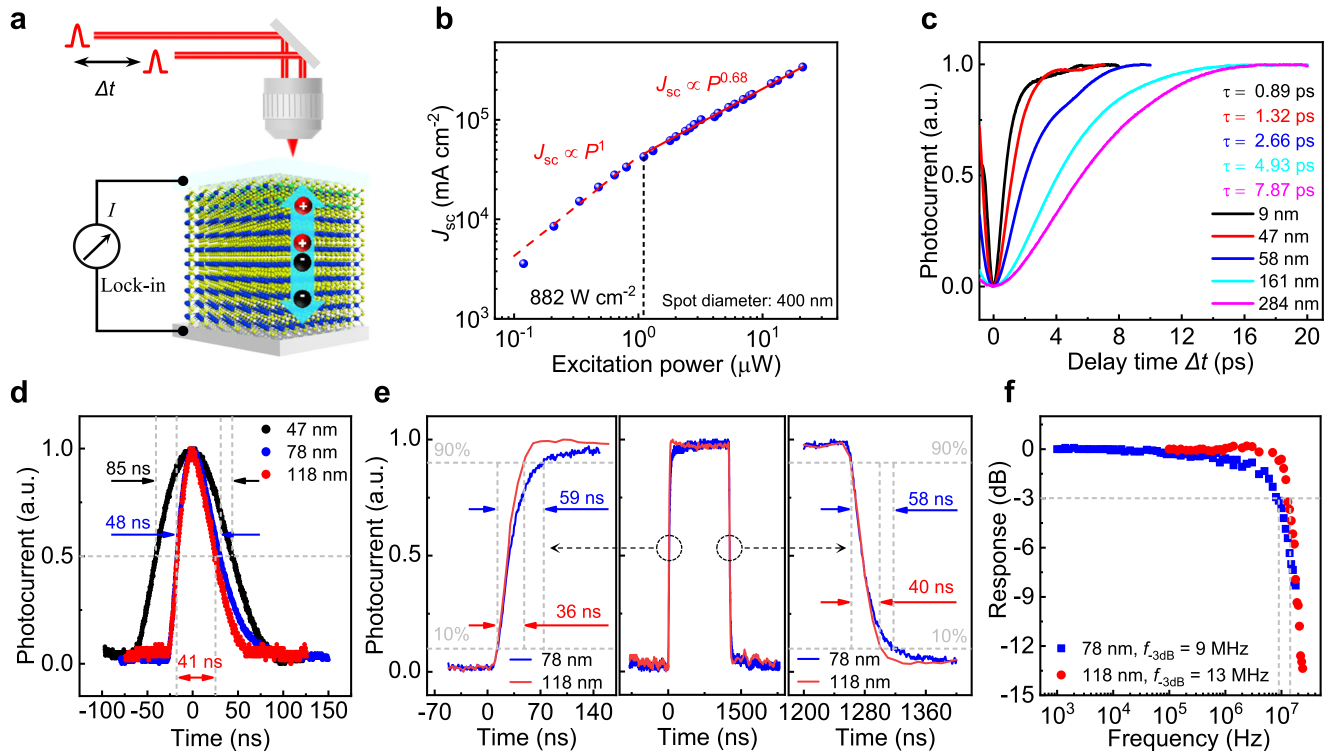

Fig. 3 | Intrinsic response time and switching response time of the vertical WSe_2 p-i-n photodiode. a Schematic illustration of time-resolved photocurrent measurement (TRPC) by 780 nm pulsed laser (80 fs) at V_{ds} = 0 V. The Δt represents the delay time between pump and probe beams. Under pulsed laser excitation and built-in electric field, photogenerated electron-hole pairs are created, separated, and transported to the metal electrodes. **b** Short-circuit photocurrent density (J_{sc}) as a function of probe beam power without pump beam. The red dash and solid lines are the power-law fits with $J_{ph} \propto P^1$ and $J_{ph} \propto P^{0.68}$, respectively. The linear-to-sublinear transition occurs at P = 882 W cm^{-2}. **c** TRPC measurements of the p-i-n devices with different WSe_2 thicknesses. **d** Normalized transient photoresponse under 266 nm pulsed laser with different thicknesses of pristine WSe_2. Response time extracted from the full width at half maximum of the response curve. **e** Photoswitching behaviors of the WSe_2 p-i-n photodiodes under 532 nm laser at V_{ds} = 0 V and laser on/off switching frequency of 400 kHz. The switching response time is the time that photocurrent rises from 10% to 90% or falls from 90 to 10% of the peak. **f** Broadband frequency response of the vertical WSe_2 p-i-n photodiode. The gray dash lines show the bandwidth when the amplitude of the normalized photoresponse drops by −3 dB (the frequency that photocurrent reduces to 0.707 of the maximum value).

at V_{ds} = 0 V (Fig. 3c). The photoresponse characteristics of the samples are shown in Supplementary Fig. 13. Assuming that the photogenerated V_{oc} is equal to the built-in potential V_{bi} (in fact, V_{oc} is usually smaller than V_{bi}), the estimated built-in electric field strengths from 9 nm sample to 284 nm sample are 333 kV cm^{-1}, 115 kV cm^{-1}, 93.1 kV cm^{-1}, 37.3 kV cm^{-1} and 23.9 kV cm^{-1}, respectively. The intrinsic response time τ can be extracted from the photocurrent-delay time curve by the following equation[21]:

$$\frac{I_{ph}(\Delta t)}{I_{ph}(\Delta t \to \infty)} = 1 - Ae^{-\frac{\Delta t}{\tau}} \tag{2}$$

in which A and τ are the fitting parameters. When thickness is 284 nm, τ = 7.87 ps is obtained. And when L is 9 nm, τ reaches as short as 0.89 ps, which is the shortest intrinsic response time in TMDs based vertical photodetectors as far as we know[22–25], indicating the potential application of our device in high-speed and high-responsivity detectors.

The intrinsic response time from TRPC technology is composed of drift time τ_{drift}, recombination time τ_r, exciton dissociation time and interface transfer time τ_s, and there is the specific relationship[22,26]:

$$\Gamma = \frac{1}{\tau} = \frac{1}{\tau_{drift} + \tau_s} + \frac{1}{\tau_r} \tag{3}$$

By varying the i-WSe_2 thicknesses in vertical p-i-n photodiodes, we plot Γ with E/L (Supplementary Fig. 14) and extract τ_s of 0.884 ps, τ_r of 11.1 ps, the mobility of 16.2 cm^{2}V^{-1}s^{-1}, and the carriers drift velocity of >10^6 cm/s, approaching the saturation drift velocity of WSe_2[27]. Overall, our results show that the degenerate doping and the vertical structure with short channels contribute to the high-field velocity transport and the short intrinsic response time.

Different from the intrinsic response measurement, which provides the upper speed limit of photoresponse, the extrinsic switching response time is actual response time of photodiode, indicating the ability of a photodetector to process high frequency signals. To test the switching response time, the devices are manually soldered and bonded to a homemade PCB board, and the response time is obtained by connecting the transimpedance amplifier and the oscilloscope. We conducted photocurrent - time (I-t) tests using 266 nm pulsed laser (Fig. 3d) and 532 nm continuous laser (Fig. 3e). The switching response time decreases with the increasing WSe_2 thickness. When the thickness is 118 nm, the switching response time is 36 ns, which is quite fast in TMDs based photodetectors[28–33]. The full cycles of the two samples under 532 nm laser illumination are shown in Supplementary Fig. 15. In addition, we tested the broadband frequency response of vertical p-i-n devices from 1 kHz to 25 MHz. The 3 dB cutoff frequency of 9 MHz is obtained in 78-nm-thick devices. And the 3 dB cutoff frequency increases to 13 MHz in 118-nm-thick devices (Fig. 3f). Based on the results from three different characterization methods, we concluded that as the thickness increases (or junction capacitance decreases), the device response time decreases. The relation between junction capacitance (C) and switching response time (t_{ex}) follows the function of $t_{ex} \propto C^{1.04}$ (Supplementary Fig. 16). In addition, it has been demonstrated

that the test board and the transimpedance amplifier (TIA) seriously affect the response time of the device (Supplementary Fig. 17)[34]. Therefore, the obtained response time is limited by the test setup and the actual response time of p-i-n device should be faster.

We fabricated a vertical graphene/WSe_2/Ar-WSe_2 p-i-n photodiode as a control device. The J–V characteristics of the photodiode under 808 nm laser illumination and the photoswitching behaviors are shown in Supplementary Fig. 18. The device exhibits a saturated open-circuit voltage V_{oc} of 0.24 V when the optical power density is over 757 mW·cm^{-2} and a long rise/fall time of 10 µs/6.5 µs. The extracted contact (series) resistance is as large as 8 MΩ, and several control devices all exhibit high contact resistance (Supplementary Fig. 19), leading to a high RC time delay and a reduced voltage drop across the intrinsic region. From the statistical analysis of the response times (Supplementary Fig. 18), we can conclude that the difference in contact resistance causes a significant variation in the response speed. Therefore, a degenerate doping layer can reduce the contact resistance and increase the built-in electric field, which is crucial for a high-speed vertical WSe_2 p-i-n photodiode.

Downscaling p-type layer thickness to approach ideal efficiency

To resolve the dilemma in the vertical WSe_2 p-i-n photodiode in terms of speed and responsivity, we need to improve the external quantum efficiency (EQE) expressed in the number of photogenerated carriers collected per incident photon. The ideal condition is that the light is completely absorbed by the intrinsic WSe_2 layer and the photogenerated carriers are efficiently separated by the built-in electric field without recombination. However, the heavily doped layer on top can also absorb the light and the photogenerated carriers at the doped layer have to diffuse into the depletion region. In fact, most of the photogenerated carriers at the doped layer quickly recombine and result in a noticeable decrease in the EQE and responsivity, as depicted in Fig. 4a. In our work, the thickness of the p-type Nb-WSe_2 layer can be downscaled to sub-10 nanometers and even sub-1 nanometer[35,36].

To investigate the effect of p-type layer thickness on the optical response characteristic, we vary the p-type Nb-WSe_2 layer thickness from 9 nm to 128 nm (Supplementary Fig. 20). Figure 4b presents the photocurrent density J_{ph} - V_{ds} curves of vertical p-i-n photodiodes dependent on the Nb-WSe_2 thicknesses under a constant power density (10 mW·cm^{-2}) of 532 nm laser. As the thickness of Nb-WSe_2 decreases from 128 nm to 9 nm, J_{ph} of the photodiode at $V_{ds} = 0$ V gradually increases from 2×10^{-12} A·µm^{-2} to 2.8×10^{-11} A·µm^{-2}. Responsivity (R) is calculated by J_{ph}/P_{in}, in which P_{in} is the incident laser power density. The increased photocurrent density under a constant laser power density indicates the boosted responsivity. The photoresponse curves and the responsivity as a function of incident power density for four samples are shown in Supplementary Fig. 20. It can be seen that, as the Nb-WSe_2 thickness decreases, the responsivity significantly increases. Figure 4c shows the dependence of the responsivity and EQE on the Nb-WSe_2 thicknesses. The responsivity increases from 21.36 mA W^{-1} to 298.87 mA W^{-1} with the decreased thickness of Nb-WSe_2. The EQE is extracted through $hCJ_{ph}/q\lambda P_{in}$, where h is the Planck constant, C is speed of light, q is elementary charge, and λ is wavelength. EQE exhibits the same trend as the responsivity, which increases from 4.98 to 69.67%.

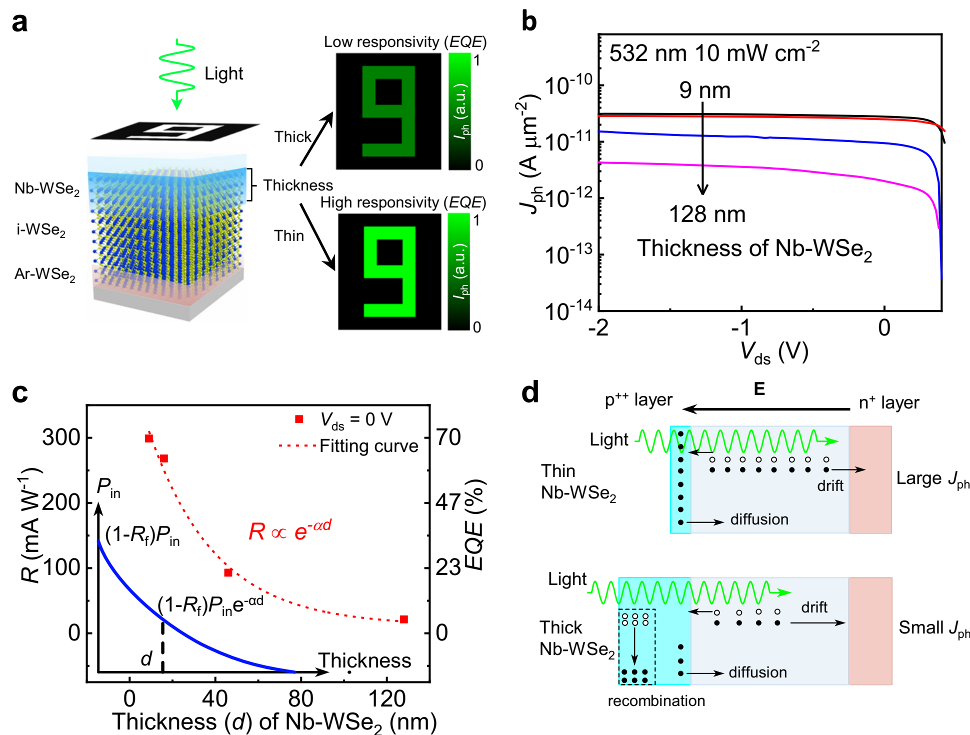

Fig. 4 | Downscaling of Nb-WSe_2 thickness to boost responsivity and quantum efficiency. a Schematic of the p-type layer thickness effect in the WSe_2 p-i-n photodiode. Thick Nb-WSe_2 exhibits high carrier recombination, leading to reduced responsivity. In contrast, thin Nb-WSe_2 minimizes top-layer absorption while suppressing carrier recombination, achieving enhanced responsivity. **b** J_{ph} - V_{ds} curves of p-i-n photodiode under 532 nm laser illumination with different Nb-WSe_2 thicknesses. **c** Responsivity (R) and external quantum efficiency (EQE) as a function of Nb-WSe_2 thickness (d). The responsivity exhibits exponential decay with increasing d, following the relation: $R = 398.84 \times e^{-d/31.13} + 11.67$, responsivity is the average value under different powers. Inset is the optical power density P_{in} as a function of d in p-i-n photodiode, R_f is reflection at the surface, α is the light absorption coefficient of the material. The maximum optical power that i-WSe_2 can absorb is $(1-R_f)\,P_{in}\,e^{-\alpha d}$. **d** Schematic of light absorption in the p-i-n photodiodes with thin and thick Nb-WSe_2. Thick Nb-WSe_2 exhibit strong optical absorption, most photogenerated carriers undergo rapid recombination, significantly reducing the photocurrent density (J_{ph}) in i-WSe_2. In contrast, thin Nb-WSe_2 permits effective carrier diffusion into i-WSe_2 while allowing majority light absorption to occur in i-WSe_2, thereby substantially enhancing the photocurrent density.

We further find that the responsivity-thickness curve fits well with an exponential decay function (Fig. 4c). Theoretically, the responsivity can be expressed as

$$R = \frac{q\lambda}{hc}(1 - R_f)\eta e^{-\alpha d} \tag{4}$$

in which R_f is the reflection at the surface, α is the light absorption coefficient of the material, η is the internal quantum efficiency, and d is the p-type layer thickness. At $V_{ds} = 0$ V, responsivity is fitted as $R = 398.84 \times e^{-d/31.13} + 11.67$. We can obtain $\alpha = 3.21 \times 10^5 \mathrm{cm}^{-1}$, which is close to the WSe_2 absorption coefficient of $3.38 \times 10^5 \mathrm{cm}^{-1}$ in literatures[11].The decreased responsivity and *EQE* with the increased thickness of p-type layer can be explained by the exponential increase of light absorption by the p-type layers. Before light reaches i-WSe_2, it attenuates due to the absorption by Nb-WSe_2. The maximum light intensity that pristine WSe_2 can absorb is given by $(1\text{-}R_f)P_{in}e^{-\alpha d}$ (inset of Fig. 4c). Moreover, only a small portion of the photogenerated carriers produced by Nb-WSe_2 near the interface will diffuse into the depletion region, while the rest will recombine quickly. Therefore, the thinner the Nb-WSe_2 layer, the smaller the recombination probability, resulting in a greater number of photo-generated carriers produced in the intrinsic region, and consequently, a higher photocurrent density, responsivity and *EQE*, as shown in Fig. 4d.

Due to the high carrier density of doped WSe_2 and the limited carrier density of pristine WSe_2 ($6.56 \times 10^{14} \mathrm{cm}^{-3}$), the monolayer Nb-$WSe_2$ can induce the depletion of 1275-nm-thick pristine WSe_2 at $V_{ds} = 0$ V (Supplementary Note 2 and 3). We can infer that the use of monolayer Nb-WSe_2 with the thickness of 0.7 nm (refs. 37,38) can further increase responsivity and *EQE* to 401.6 mA W^{-1} and 93.6%, respectively, while ensuring full depletion of the intrinsic layer and complete absorption of 532 nm laser (10 mW·cm^{-2}). Therefore, to simultaneously achieve high responsivity and fast speed, it is required to use ultrathin Nb-WSe_2 and select a relatively thick intrinsic WSe_2 layer under the premise of full depletion (reduced RC time delay).

Figures of merit in vertical WSe_2 p-i-n photodiodes

After the systematic discussion of dominant limiting factors on the photodiode performance, we fabricated the optimized vertical Nb-WSe_2/WSe_2/Ar-WSe_2 p-i-n photodiode with ohmic contact and ultrathin Nb-WSe_2 top layer, which enables high efficiency and ultrafast response. The thickness of WSe_2 and Nb-WSe_2 is 307 nm and 4.5 nm, respectively (Supplementary Fig. 21). Figure 5a presents the power dependent photoresponse. Under dark, the current rectification ratio of the p-i-n photodiode is 6×10^6 ($V_{ds} = \pm 2$ V). As the P_{in} increases, both the J_{sc} and V_{oc} significantly increase (Fig. 5b). At the P_{in} of 612 mW·cm^{-2}, the ratio of J_{sc} to dark current density (J_{sc}/J_{dark}) exceeds 10^6, indicating an extremely high signal-to-noise ratio.

To describe the linearity of the photodiode, the linear dynamic range (*LDR*) is introduced, which can be calculated by the equation[39]

$$LDR = 10 \times \log_{10}\left(\frac{P_{max}}{P_{min}}\right) \tag{5}$$

in which P_{min}/P_{max} is the lowest/highest laser power density of the linear region. It should be emphasized that when calculating *LDR* using optical power, $10\log_{10}$ should be used instead of $20\log_{10}$ which is widely misused. The p-i-n photodiodes show high linearity in a power range of more than five orders of magnitude under 532 nm laser illumination (Fig. 5b). To obtain the *LDR* limitation of our device, we test *LDR* under 808 nm laser with a larger power range. The *LDR* of p-i-n photodiodes in our study exceeding 75 dB, which is close to commercial Si photodiodes (approximately 80 dB for S1133 from Hamamatsu)[40]. It is worth noting that the *LDR* of our device can

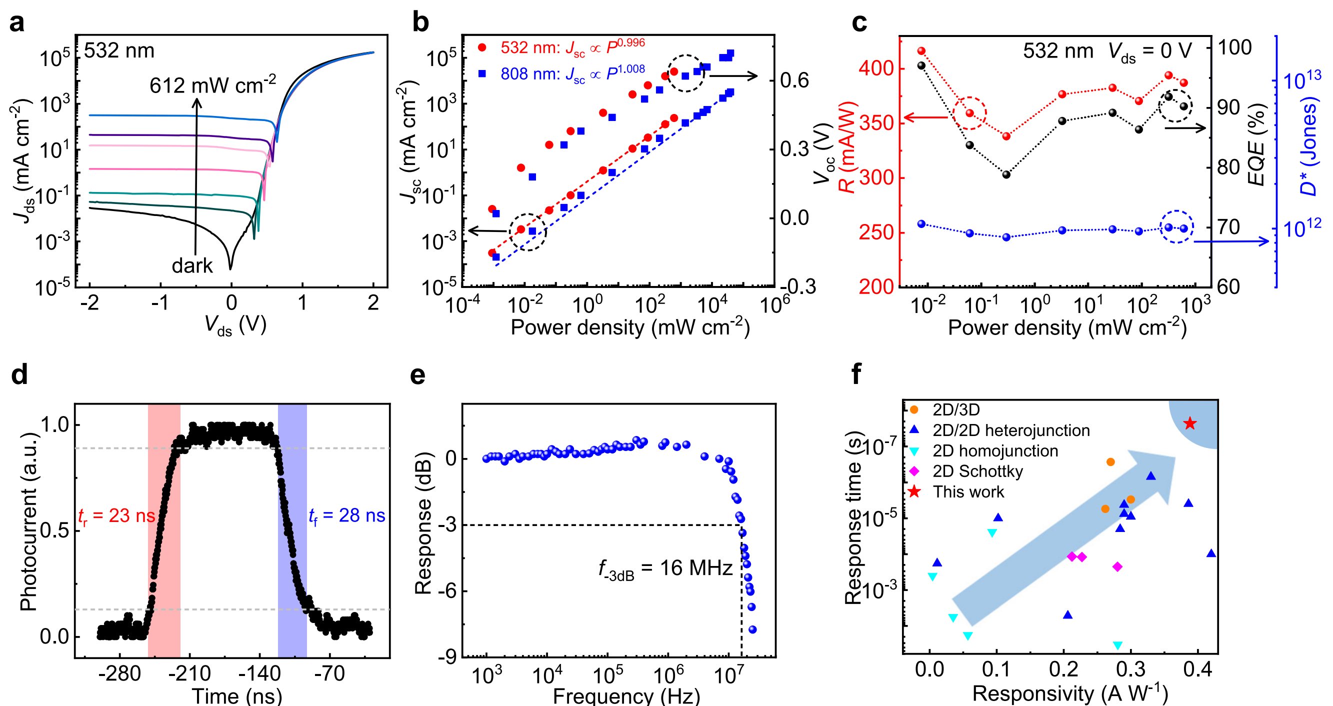

Fig. 5 | Optoelectronic characteristics of the optimized WSe_2 p-i-n photodiode. **a** J_{ds}-V_{ds} curves under 532 nm laser illumination with different power densities. **b** J_{sc} and V_{oc} as a function of incident power density under 532 nm and 808 nm laser illumination. The power-law fits between J_{sc} and power density are $J_{ph} \propto P^{0.996}$ (532 nm) and $J_{ph} \propto P^{1.008}$ (808 nm), respectively. **c** Responsivity (*R*), external quantum efficiency (*EQE*) and specific detectivity (*D**) as a function of 532 nm incident light power density at $V_{ds} = 0$ V. **d** Photoswitching behavior of the vertical WSe_2 p-i-n photodiode at $V_{ds} = 0$ V and laser on/off switching frequency of 4 MHz. The gray dash lines represent the 10% and 90% positions of the switch. **e** Broadband frequency response of the vertical WSe_2 p-i-n photodiode at $V_{ds} = 0$ V. **f** Responsivity and response time comparison under self-powered mode with previous reports. For visible detector, the vertical WSe_2 p-i-n photodiode shows high responsivity and fast speed. (Supplementary Table 1, for more details and references).

be even higher since the power range of P_{in} can be further expanded. We also calculated the *LDR* of the control photodiodes (graphene/WSe_2/Ar-WSe_2). The average value is 24 dB, which is 10^5 times smaller than that of the p-i-n photodiode, as shown in Supplementary Fig. 22. The *LDR* of the control photodiode is greatly affected by the intrinsic hot carrier dynamics of graphene and the large contact resistance[39]. In our p-i-n photodiodes, the high doping concentration of Nb-WSe_2 and Ar-WSe_2 results in a small contact resistance, achieving a high *LDR*.

The responsivity and *EQE* of the vertical p-i-n photodiode under visible light and varied power density at V_{ds} of 0 V are shown in Fig. 5c and Supplementary Fig. 23. The responsivity can be as high as 388.0 mA W^{-1} (*EQE* of 90.5%) at 532 nm, and 0.554 A W^{-1} (*EQE* ~ 91.6%) at 750 nm, which is outperforming commercial silicon photodiodes[40]. The responsivity and *EQE* of our device at zero bias are outstanding among 2D p-i-n homojunction[41–43], demonstrating high sensitivity and self-powered detection capabilities.

To comprehensively evaluate the detector's ability to sense weak signals, we assess the specific detectivity (D^*). D^* can be given by the expression[22]

$$D^* = \frac{\sqrt{S}}{NEP} \tag{6}$$

$$NEP = \frac{1}{R}\sqrt{2qI_{dark} + \frac{4k_BT}{R_{sh}}} \tag{7}$$

where S is the effective area, k_B is the boltzmann constant, T is the temperature, R_{sh} is shunt resistance. Figure 5c plots D^* with incident laser power density, displaying negligible dependency. At V_{ds} of 0 V, the D^* is 1×10^{12} Jones, close to the commercial Si photodiode. The high D^* at V_{ds} of 0 V can be attributed to the ultralow thermal noise, which replaces shot noise as the dominant source of total noise. Supplementary Fig. 23 also shows R, *NEP* and D^* as a function of power density and V_{ds}.

To ascertain the response time, we monitored the temporal switching response with the incident light being alternately switched on and off at a frequency of 4 MHz. Figure 5d shows one cycle of photoswitching, operating at V_{ds} = 0 V. The rise and fall time are 23 ns and 28 ns, respectively. Figure 5e shows the normalized AC photoresponse in a broad frequency range from 1 kHz to 25 MHz. From the variation in the relative amplitude of the photoresponse, a 3 dB cutoff frequency of 16 MHz is obtained. As summarized in Fig. 5f and Supplementary Table 1, without voltage bias, our vertical p-i-n photodiodes achieve near-ideal external quantum efficiency while maintaining fast response speed, outperforming most self-powered photodetectors based on TMDs[44–46] and even commercial Si photodiodes. We can further estimate the theoretical minimum response time of the device by using RC time and TRPC test results, which is 200.4 ps (Supplementary Fig. 24).

The photovoltaic performance can also demonstrate the photocarrier generation and transfer dynamics in p-i-n photodiodes. To achieve high power conversion efficiency (*PCE*), it requires the strong absorption by the intrinsic layer and the effective separation of photogenerated carriers with minimized recombination[47,48]. Hence, we systematically evaluate the photovoltaic performance of our optimized vertical p-i-n photodiodes. Figure 6a displays the J_{ds}-V_{ds} curves in the linear scale under dark and 532 nm laser illumination, respectively. A large V_{oc} of 0.62 V and a high J_{sc} of 125.7 mA cm^{-2} are obtained

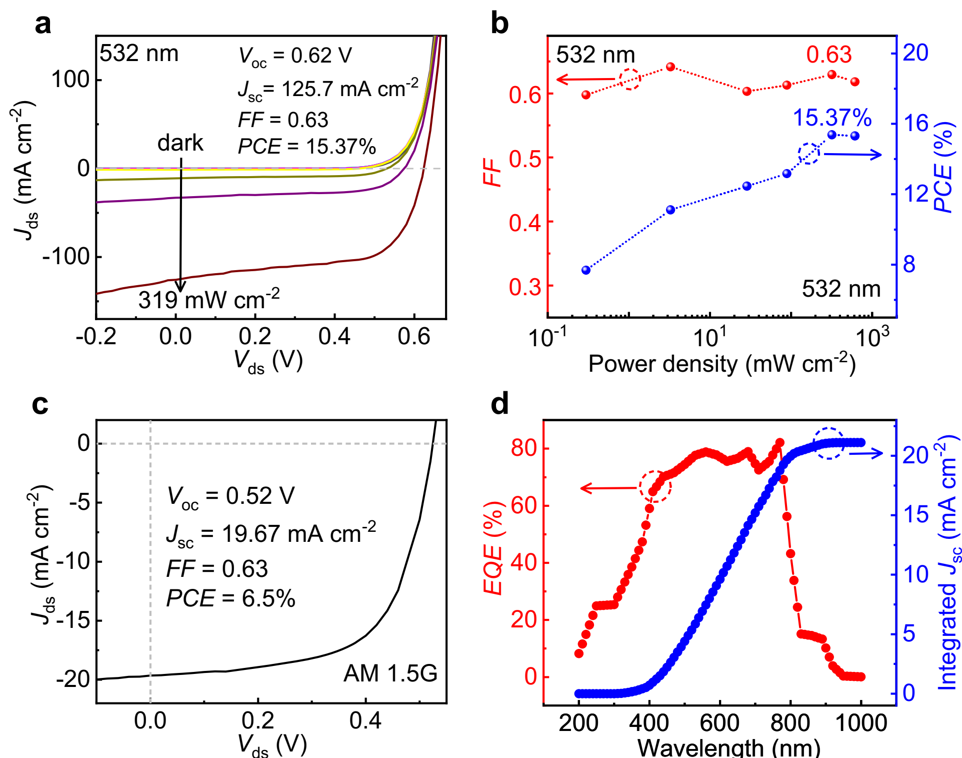

Fig. 6 | Photovoltaic characteristic of the optimized WSe_2 p-i-n photodiode. **a** Linear J_{ds} - V_{ds} curves of the WSe_2 p-i-n photodiode under 532 nm laser illumination with varied power densities. Inset is the value of V_{oc}, J_{sc}, *FF* and *PCE* when *PCE* is maximum. **b** Fill factor (*FF*) and power conversion efficiency (*PCE*) as function of power density under 532 nm laser illumination. The maximum *PCE* is 15.37%, corresponding *FF* is 0.63. **c** Linear J_{ds} - V_{ds} curve of the WSe_2 p-i-n photodiode under AM 1.5 G illumination. Inset is the value of V_{oc}, J_{sc}, *FF* and *PCE*. **d** Spectral *EQE* at V_{ds} = 0 V and integrated short current density. The spectral response is measured under Xenon lamp.

under the power density of 319 mW cm^{-2}. We can extract the fill factor (FF) and PCE using the following equation[49]

$$FF = \frac{(P_{el})_{max}}{V_{oc} \times I_{sc}} \quad (8)$$

$$PCE = \frac{(P_{el})_{max}}{P_{in}} \quad (9)$$

where P_{el} is the output electrical power defined as $P_{el} = V_{ds} \times I_{ds}$. As P_{el} describes the power generation capability of a photovoltaic device, we need to achieve the maximum P_{el} at a certain voltage bias. Supplementary Fig. 25 illustrates the relationship between P_{el} and V_{ds} under 532 nm laser irradiation. Figure 6b shows that our device displays a maximum PCE of 15.37% and a maximum FF of 0.63 under P_{in} of 319 mW cm^{-2}.

To benchmark with other photovoltaic devices, we investigate the photovoltaic performances of vertical WSe_2 p-i-n photodiode under 1000 W m^{-2} air mass 1.5 global (AM 1.5 G) illumination. We test the forward and reverse current density–voltage curve (Supplementary Fig. 26), the device exhibits negligible hysteresis. The device with an area of 1022 μm^2 obtains V_{oc} of 0.52 V, J_{sc} of 19.67 mA cm^{-2}, FF of 0.63, and PCE of 6.5% (Fig. 6c). EQE characterization under different wavelengths was further performed to confirm the measured J_{SC} (Fig. 6d). The integrated J_{sc} is 21.1 mA cm^{-2}, which is closed to the measured J_{SC} under the solar simulator. Under AM 1.5 G illumination, our vertical WSe_2 p-i-n device demonstrates excellent performance among TMDs-based photovoltaic devices (Supplementary Table 2). Compared with ultrathin silicon photovoltaics, the PCE of our device is higher than that of silicon at the same thickness[50], which is attributed to the effective separation/collection of carriers in the p-i-n structure under high built-in electric field and the high light absorption coefficient of WSe_2. Due to the narrow absorption spectrum of WSe_2 (mainly visible light), PCE of our device can be further improved by selecting other 2D layers with appropriate bandgap engineering.

Discussion

Overall, we have fabricated vertical WSe_2 p-i-n photodiodes with ultrathin degenerate p-doped Nb-WSe_2 layer, enabling fast response speed and high quantum efficiency. The Nb-WSe_2 layer with high hole concentration of 2.65×10^{21} cm^{-3} effectively reduces the contact resistance and increases the built-in electric field, resulting in the fast response speed. Due to the 2D nature of Nb-WSe_2, the thickness can be downscaled to sub-10 nm, leading to the high responsivity and quantum efficiency. The optimized WSe_2 p-i-n photodiodes with ultrathin Nb-WSe_2 exhibit strong rectifying behavior with a current on/off ratio of approximately 6×10^6. The p-i-n photodiode demonstrates high self-powered photodetection performance with a high open-circuit voltage of 0.62 V and a nearly ideal linearity of the short-circuit current, achieving a high LDR up to 75 dB. And the device displays a high responsivity of 388.0 mA W^{-1} (EQE of 90.5%), a specific detectivity of 1×10^{12} Jones, a high power conversion efficiency of 6.5%, a fast 10-picosecond intrinsic response time, and a fast switching response time of 23 ns. Such self-powered optoelectronic performance positions our vertical WSe_2 p-i-n photodiodes with great prospects in fast signal detection, high resolution imaging, low power consumption, and photovoltaic applications.

Methods

Materials

Bulk pristine WSe_2 crystals were purchased from Shanghai Onway Technology Co., Ltd and Nb doped WSe_2 crystals (Nb: 5%) were purchased from Sixcarbon Technology, respectively.

Device fabrication and characterization

The vertical WSe_2 p-i-n photodiodes were fabricated by a commonly used dry transfer method utilizing polydimethylsiloxane (PDMS) film. First, Ag bottom electrode was deposited on SiO_2/Si substrate (t_{ox} = 285 nm). Then, pristine WSe_2 flakes were mechanically exfoliated by the Scotch-tape method and transferred to PDMS. The argon (Ar) plasma treatments were performed on the pristine WSe_2 at a pressure of 5 Pa, a power of 100 W, a gas flow of 50 sccm, and a duration time of 90 s, which achieves n-type doping by bombarding WSe_2 to generate abundant Se vacancies. Next, the surface treated WSe_2 were transferred onto the Ag bottom electrodes. Nb-WSe_2 flakes were mechanically exfoliated by the Scotch-tape method and transferred to PDMS, and then transferred onto the pristine WSe_2 flakes to form p-i-n homojunction. The detailed fabrication process is shown in Supplementary Fig. 9. The flake thickness was confirmed by Atomic Force Microscopy (Bruker).

Electrical and photoresponse measurements

All electrical and photoelectric tests were performed at room temperature and ambient pressure. The current density-voltage (J–V) measurements of the p-i-n photodiodes were characterized by a Keithley 2636B sourcemeter. For the test of the extrinsic response time and frequency response, a 266 nm pulsed laser (pulse duration ~6 ns) and 532 nm laser with electro-optic modulator (up to 25 Mhz) was used selected, the frequency of which was modulated by a function generator. The signal of the photoelectric conversion was first amplified by a transimpedance amplifier (Femto DHPCA-100, the rise time is 4.4 ns at gain of 10^3) and then fed into the high-speed oscilloscope (RIGOL, MSO8104) to read the time of rise and fall. In other photoresponse measurements, 532 nm and 808 nm continuous laser were selected, the laser spot displays a diameter of about ~200 μm, larger than the device area to make sure a uniform illumination.

The calculation of carrier density

The pristine carrier density in bulk concentration n_{3D} can be calculated based on the following equation: $n_{3D} = \frac{n_{2D}}{d}$, 2D$concentration n_{2D} = \frac{\sigma_{2D}}{q\mu}$, 2Dconductivity$\sigma_{2D} = \frac{I_{ds}}{\Delta V}\frac{L}{W}$, field-effect mobility $\mu = \frac{d\sigma_{2D}}{dV_{bg}} \times \frac{1}{C_{ox}}$, where d is the thickness of material, q is the elementary charge, I_{ds} is the source-drain current, ΔV is the voltage drop between the two contacts, L/W is the length/width ratio of the channel, C_{ox} is the capacitance of dielectric per unit area (1.21×10^{-8} F/cm^2 for 285 nm SiO_2). Furthermore, The Ar plasma induced charge density could be extracted by $\Delta n_{2D} = C_{ox}\frac{\Delta V_{th}}{q}$, where the ΔV_{th} is the threshold voltage variation induced by Ar plasma.

Hall effect and TEM measurement

Carrier concentration of Nb-WSe_2 is determined by the Hall Effect system (Nanometrics HL5500), which is based on van der Pauw Method. For TEM, sample was prepared using a FEI Quanta 3D FEG dual-beam system. TEM imaging was conducted in a Hitachi H-9500 (300 kV) transmission electron microscope.

SPCM and TRPC measurements

In SPCM measurements, a 488 nm continuous-wave laser was chopped by a mechanical chopper at 1050 Hz and then focused onto the sample by a long working distance objective (Olympus LMPLFLN 50×) near the diffraction limit. The generated photocurrent was collected by a lock-in amplifier (Stanford SR830) at the chopped frequency with a background noise of ≈0.2 pA. The SPCM measurements with a resolution close to the diffraction limit were performed by raster scanning the entire device mounted on a piezoelectric translation stage (Piezoconcept LT3) according to the fixed laser spot. In TRPC measurements, a 780 nm pulse laser (diameter ~400 nm) was split into two independent beams to form a pump–probe measurement configuration, and the probe beam was chopped so that the lock-in amplifier could only

measure its photocurrent. The pump beam was delayed by different path lengths, with the delay time precisely controlled by a mechanical delay stage (Thorlabs DDSM100/M). The pump and probe beams were recombined by a beam splitter after the delay line stage and focused onto the sample using the same long working distance objective. The temporal resolution of the TRPC set-up was about 0.6 ps.

AM 1.5 G measurement

The *J*–*V* characteristics of the p-i-n photovoltaic performance were measured using a Keithley 2400 sourcemeter under a simulated AM 1.5 G spectrum, with an Oriel 9600 solar simulator. The devices were measured in both reverse and forward scan (−0.1 V to 0.6 V, step 0.02 V). All the devices were measured without preconditioning such as light soaking or a bias voltage.

Reporting summary

Further information on research design is available in the Nature Portfolio Reporting Summary linked to this article.

Data availability

Source data are provided with this paper. All raw data generated during the current study are available from the corresponding authors upon request.

References

1. Xia, F., Wang, H., Xiao, D., Dubey, M. & Ramasubramaniam, A. Two-dimensional material nanophotonics. *Nat. Photon.* **8**, 899–907 (2014).
2. Koppens, F. H. L. et al. Photodetectors based on graphene, other two-dimensional materials and hybrid systems. *Nat. Nanotechnol.* **9**, 780–793 (2014).
3. Darweesh, R. et al. Nonlinear self-calibrated spectrometer with single GeSe-InSe heterojunction device. *Sci. Adv.* **10**, eadn6028 (2024).
4. Ma, C. et al. Intelligent infrared sensing enabled by tunable moiré quantum geometry. *Nature* **604**, 266–272 (2022).
5. Yu, W. J. et al. Highly efficient gate-tunable photocurrent generation in vertical heterostructures of layered materials. *Nat. Nanotechnol.* **8**, 952–958 (2013).
6. Pham, P. V. et al. 2D heterostructures for ubiquitous electronics and optoelectronics: principles, opportunities, and challenges. *Chem. Rev.* **122**, 6514–6613 (2022).
7. Schinke, C. et al. Uncertainty analysis for the coefficient of band-to-band absorption of crystalline silicon. *AIP Adv.* **5**, 067168 (2015).
8. Britnell, L. et al. Strong light-matter interactions in heterostructures of atomically thin films. *Science* **340**, 1311–1314 (2013).
9. Liu, Y. et al. Approaching the Schottky–Mott limit in van der Waals metal–semiconductor junctions. *Nature* **557**, 696–700 (2018).
10. Chen, P. et al. Approaching the intrinsic exciton physics limit in two-dimensional semiconductor diodes. *Nature* **599**, 404–410 (2021).
11. Zotev, P. G. et al. Van der Waals materials for applications in nanophotonics. *Laser Photon. Rev.* **17**, 2200957 (2023).
12. Memaran, S. et al. Pronounced photovoltaic response from multi-layered transition-metal dichalcogenides PN-Junctions. *Nano Lett.* **15**, 7532–7538 (2015).
13. Le Thi, H. Y. et al. Doping-free high-performance photovoltaic effect in a WSe_2 lateral *p-n* homojunction formed by contact engineering. *ACS Appl. Mater. Interfaces* **15**, 35342–35349 (2023).
14. Tsai, M. et al. Single atomically sharp lateral monolayer p-n heterojunction solar cells with extraordinarily high power conversion efficiency. *Adv. Mater.* **29**, 1701168 (2017).
15. Zhang, Y. et al. High-speed transition-metal dichalcogenides based schottky photodiodes for visible and infrared light communication. *ACS Nano* **16**, 19187–19198 (2022).
16. Xu, Q. et al. Ultrafast colloidal quantum dot infrared photodiode. *ACS Photon.* **7**, 1297–1303 (2020).
17. Deng, Y. et al. Short-wave infrared colloidal QD photodetector with nanosecond response times enabled by ultrathin absorber layers. *Adv. Mater.* **36**, 2402002 (2024).
18. Yamamoto, M., Nakaharai, S., Ueno, K. & Tsukagoshi, K. Self-limiting oxides on WSe_2 as controlled surface acceptors and low-resistance hole contacts. *Nano Lett.* **16**, 2720–2727 (2016).
19. Arnold, A. J., Schulman, D. S. & Das, S. Thickness trends of electron and hole conduction and contact carrier injection in surface charge transfer doped 2D field effect transistors. *ACS Nano* **14**, 13557–13568 (2020).
20. Choi, M. S. et al. High carrier mobility in graphene doped using a monolayer of tungsten oxyselenide. *Nat. Electron.* **4**, 731–739 (2021).
21. Zeng, Z. et al. Dual polarization-enabled ultrafast bulk photovoltaic response in van der waals heterostructures. *Nat. Commun.* **15**, 5355 (2024).
22. Massicotte, M. et al. Picosecond photoresponse in van der Waals heterostructures. *Nat. Nanotechnol.* **11**, 42–46 (2016).
23. Wu, J. et al. Ultrafast response of spontaneous photovoltaic effect in 3R-MoS_2–based heterostructures. *Sci. Adv.* **8**, eade3759 (2022).
24. Zeng, Z. et al. Manipulating picosecond photoresponse in van der waals heterostructure photodetectors. *Adv. Funct. Mater.* **32**, 2200973 (2022).
25. Gabor, N. M., Zhong, Z., Bosnick, K. & McEuen, P. L. Ultrafast photocurrent measurement of the escape time of electrons and holes from carbon nanotube p-i-n photodiodes. *Phys. Rev. Lett.* **108**, 087404 (2012).
26. Massicotte, M. et al. Dissociation of two-dimensional excitons in monolayer WSe_2. *Nat. Commun.* **9**, 1633 (2018).
27. Zhang, C., Cheng, L. & Liu, Y. Understanding high-field electron transport properties and strain effects of monolayer transition metal dichalcogenides. *Phys. Rev. B* **102**, 115405 (2020).
28. Gong, C. et al. Electronic and optoelectronic applications based on 2D novel anisotropic transition metal dichalcogenides. *Adv. Sci.* **4**, 1700231 (2017).
29. Liu, M. et al. Photogating-assisted tunneling boosts the responsivity and speed of heterogeneous WSe_2/Ta_2NiSe_5 photodetectors. *Nat. Commun.* **15**, 141 (2024).
30. Tsai, M.-Y. et al. Ultrafast and broad-band graphene heterojunction photodetectors with high gain. *ACS Nano* **17**, 25037–25044 (2023).
31. Xin, W. et al. Low-dimensional-materials-based photodetectors for next-generation polarized detection and imaging. *Adv. Mater.* **36**, 2306772 (2024).
32. Hu, T. et al. High-sensitivity and fast-speed UV photodetectors based on asymmetric nanoporous-GaN/graphene vertical junction. *ACS Nano* **17**, 8411–8419 (2023).
33. Wu, F. et al. High efficiency and fast van der Waals hetero-photodiodes with a unilateral depletion region. *Nat. Commun.* **10**, 4663 (2019).
34. Wu, J. et al. High-sensitivity, high-speed, broadband mid-infrared photodetector enabled by a van der Waals heterostructure with a vertical transport channel. *Nat. Commun.* **16**, 564 (2025).
35. Park, J. et al. Nature of photoconductivity in self-powered single-atomic-layered Nb-Doped WSe_2 phototransistors. *ACS Photon.* **10**, 2930–2940 (2023).
36. Vu, V. T. et al. Synthesis of $NbSe_2$/Bilayer Nb-Doped WSe_2 heterostructure from exfoliated WSe_2 flakes. *Small Struct.* **5**, 2300401 (2024).
37. Liu, W. et al. Role of metal contacts in designing high-performance monolayer n-Type WSe_2 field effect transistors. *Nano Lett.* **13**, 1983–1990 (2013).
38. Fang, H. et al. High-performance single layered WSe_2 p-FETs with chemically doped contacts. *Nano Lett.* **12**, 3788–3792 (2012).
39. De Sanctis, A. et al. Extraordinary linear dynamic range in laser-defined functionalized graphene photodetectors. *Sci. Adv.* **3**, e1602617 (2017).

40. Fuentes-Hernandez, C. et al. Large-area low-noise flexible organic photodiodes for detecting faint visible light. *Science* **370**, 698–701 (2020).
41. Zhang, Y. et al. An ultrafast WSe_2 photodiode based on a lateral *p-i-n* homojunction. *ACS Nano* **15**, 4405–4415 (2021).
42. Li, C. et al. Waveguide-integrated $MoTe_2$ p–i–n homojunction photodetector. *ACS Nano* **16**, 20946–20955 (2022).
43. Jiang, J. et al. Polarization-resolved near-infrared $PdSe_2$ p-i-n homojunction photodetector. *Nano Lett*. **23**, 9522–9528 (2023).
44. Qiao, H. et al. Self-powered photodetectors based on 2D materials. *Adv. Opt. Mater.* **8**, 1900765 (2020).
45. Hu, X. et al. Recent progress of methods to enhance photovoltaic effect for self-powered heterojunction photodetectors and their applications in inorganic low-dimensional structures. *Adv. Funct Mater.* **31**, 2011284 (2021).
46. Ahmed, A. et al. Recent advances in 2D transition metal dichalcogenide-based photodetectors: a review. *Nanoscale* **16**, 2097–2120 (2024).
47. Li, G. et al. Highly efficient p-i-n perovskite solar cells that endure temperature variations. *Science* **379**, 399–403 (2023).
48. Jiang, Q. & Zhu, K. Rapid advances enabling high-performance inverted perovskite solar cells. *Nat. Rev. Mater.* **9**, 399–419 (2024).
49. Kim, K.-H. et al. High-efficiency WSe_2 photovoltaic devices with electron-selective contacts. *ACS Nano* **16**, 8827–8836 (2022).
50. Massiot, I., Cattoni, A. & Collin, S. Progress and prospects for ultrathin solar cells. *Nat. Energy* **5**, 959–972 (2020).

Acknowledgements

The project was primarily supported by the National Key R&D Program of China (2022YFA1204303), the National Natural Science Foundation of China (62090030, 62090034, 62104214, 62261160574, U23A20570), the Research Grant Council of Hong Kong (CRS_PolyU502/22), the Young Elite Scientists Sponsorship Program by CAST (2021QNRC001), the Kun-Peng Program of Zhejiang Province. We thank ZJU Micro-Nano Fabrication Center and ZJU-Hangzhou Global Scientific and Technological Innovation Center for the supports. We thank Prof. Wee-Liat Ong, Prof. Jingjing Xue and Prof. Lijian Zuo for the instrument support.

Author contributions

M.T. and Y.Z. conceived the idea and proposed the research. M.T. performed most of the experiments. Y.W., T.Z., C.Z., J.M., Z.B., X.S., Z.L., J.C., A.W., F.W., B.Y. and Y. X. provided experimental and methodological guidance. Y.W. carried out the TRPC and SPCM measurements and performed data analysis. M.T. wrote the manuscript. Y. C., X.W. and Y.Z. Supervise the work. All authors contributed to the general discussion.

Competing interests

The authors declare no competing interests.

Additional information

Supplementary information The online version contains supplementary material available at https://doi.org/10.1038/s41467-025-60573-z.

Correspondence and requests for materials should be addressed to Yuda Zhao.

Peer review information *Nature Communications* thanks the anonymous, reviewer(s) for their contribution to the peer review of this work. A peer review file is available.

Reprints and permissions information is available at http://www.nature.com/reprints

Publisher's note Springer Nature remains neutral with regard to jurisdictional claims in published maps and institutional affiliations.

Open Access This article is licensed under a Creative Commons Attribution-NonCommercial-NoDerivatives 4.0 International License, which permits any non-commercial use, sharing, distribution and reproduction in any medium or format, as long as you give appropriate credit to the original author(s) and the source, provide a link to the Creative Commons licence, and indicate if you modified the licensed material. You do not have permission under this licence to share adapted material derived from this article or parts of it. The images or other third party material in this article are included in the article's Creative Commons licence, unless indicated otherwise in a credit line to the material. If material is not included in the article's Creative Commons licence and your intended use is not permitted by statutory regulation or exceeds the permitted use, you will need to obtain permission directly from the copyright holder. To view a copy of this licence, visit http://creativecommons.org/licenses/by-nc-nd/4.0/.

© The Author(s) 2025